

Effects from Dark Matter Halos on X-ray Pulsar Pulse Profiles

Yukun Liu,¹ Hong-Bo Li,² Yong Gao,³ Lijing Shao,^{2,4,*} and Zexin Hu^{1,2}

¹*School of Physics, Peking University, Beijing 100871, China*

²*Kavli Institute for Astronomy and Astrophysics, Peking University, Beijing 100871, China*

³*Max Planck Institute for Gravitational Physics (Albert Einstein Institute), Am Mühlenberg 1, D-14476 Potsdam-Golm, Germany*

⁴*National Astronomical Observatories, Chinese Academy of Sciences, Beijing 100012, China*

(Dated: September 19, 2024)

Neutron stars (NSs) can capture dark matter (DM) particles because of their deep gravitational potential and high density. The accumulated DM can affect the properties of NSs. In this work we use a general relativistic two-fluid formalism to solve the structure of DM-admixed NSs (DANSs) and the surrounding spacetime. Specifically, we pay attention to the situation where those DANSs possess DM halos. Due to the gravitational effect of the DM halo, the pulse profile of an X-ray pulsar is changed. Our study finds a universal relation between the peak flux deviation of the pulse profile and $M_{\text{halo}}/R_{\text{BM}}$, which is the ratio of the DM halo mass, M_{halo} , to the baryonic matter (BM) core radius, R_{BM} . Our results show that, when $M_{\text{halo}}/R_{\text{BM}} = 0.292$ and the DM particle mass $m_f = 0.3 \text{ GeV}$, the maximum deviation of the profile can be larger than 100%, which has implication in X-ray pulsar observation.

I. INTRODUCTION

Observational evidence has increasingly supported the existence of dark matter (DM). For example, DM facilitates the formation of early galaxies [1] and helps galaxies rotate at constant speeds in their outer reaches [2]. Measurements through gravitational lensing have revealed some possible DM substructures [3]. According to our current understanding, DM occupies about a quarter of the energy density of the present Universe, while the baryonic matter (BM) only accounts for about 5% [4]. The nature of DM is a vastly uncharted territory, and exploring it can help us better understand the constitution of the Universe.

However, direct methods of searching for DM particles have not yielded satisfactory results. Thus it is of great interest to constrain the properties of DM through indirect and complementary methods. Neutron stars (NSs) provide extreme celestial laboratories for fundamental physics [5]. They may capture DM particles due to their high density and deep gravitational potential [6–13]. Even given a cross section constraint between DM and BM $\lesssim 10^{-45} \text{ cm}^2$ (say, from underground DM search experiments [14–17]), the mean free path of DM particles is still possible to be of the same order as the radius of a NS [7].

Different models of DM have different scenarios for DM-admixed NSs (DANSs) [6, 7, 18, 19]. A two-fluid model is often used for the equation of state (EOS) of DANSs [20]. In this model, one fluid is the BM while the other stands for DM, which can be asymmetric fermionic DM or self-interacting bosonic DM, and so on. After solving for the equilibrium equations, a DANS can either possess a DM core or a DM halo [8–11, 13], depending on which fluid has a larger radius. DM can significantly affect the properties of NSs. Leung *et al.* [8] demonstrated that the existence of a fermionic DM core with the DM particle mass $m_f \sim 1 \text{ GeV}$ would lower the maximum mass of NSs. Hippert *et al.* [13] showed that DANSs

may have the same mass and radius but different DM fractions. Kain [11] calculated the radical oscillation frequencies of DANSs and found that the frequencies of DANSs could be larger than the maximum possible frequencies of normal NSs. Axion DM particle stream away from NSs may transfer into photons and generate a large broadband contribution to the pulse [21]. Annihilating DM may affect the thermal conductivity and neutrino emission of NSs [22]. Numerous investigation suggests an appealing probability that NSs can be a laboratory for studying DM, concerning various observables of NSs that can be influenced by DM. To give a few examples, DM may play a role in binary systems [23–25]; radio telescope may find imprints of DM from NSs' magnetosphere [26–28]; NS surface temperature can also be impacted by DM [29, 30]. More studies on this topic can be found in Refs. [31–37].

In this work we mainly focus on the effects of DM halos on X-ray pulsar pulse profiles. A pulsar is a highly magnetized rotating NS that emits electromagnetic radiations. This radiation can only be observed when the emitting beam points to the Earth. Hot regions on a pulsar created by inward moving particles colliding with the NS surface can produce X-ray pulses, which have been observed through telescopes like the Neutron star Interior Composition ExploreR (NICER) [38–41]. The flux of the X-ray pulse changes with time, which shapes the X-ray pulse profile. It carries information related to the mass and radius of the NS [42–44]. If there is a DM halo around a NS, the pulse profile will be changed due to the gravitational effects of the massive halo. If such effects are observed, the properties of DM can be better inferred.

Miao *et al.* [45] and Shawqi and Morsink [46] showed that the X-ray profile from a pulsar can be slightly changed if a diffuse DM halo exists. In our study, we compare the pulse profile of a DANS with a NS that has the same total mass, M , and the BM core radius, R_{BM} , which—for some pulsars—are inferred observables from orbital dynamics and X-ray thermal emission, respectively [47]. Suppose that the total mass and the BM radius of a NS are obtained, we can compare its pulse profiles under the assumptions of a DANS or a normal NS. We find a universal relation between the peak flux deviation of the

* Corresponding author: lishao@pku.edu.cn

DANS pulse profiles and the ratio $M_{\text{halo}}/R_{\text{BM}}$, where M_{halo} is the mass of the DM halo. Compared with earlier studies, we consider more comprehensive models, incorporating a wider range of parameters to provide a thorough analysis of the impact of DM halos on pulse profiles. We change the position of the hot spots and the relative direction of observers, showing the fractional deviation of the peak flux as a function of the colatitude of the emitting region. In addition, we focus on extended emitting regions besides the point-like approximation, providing a more realistic representation of the actual situation. In this work, for the first time we obtain the universal relation that still holds for bosonic DM model.

The paper is organized as follows. Section II provides an introduction to the formalism used to determine the structure of DANSs and their stability. Section III briefly presents some numerical results of the structure of DANSs. Section IV outlines general methods for the calculation of pulse profiles, and shows the influence of fermionic DM halos in detail. We also extend our study to bosonic DM in this section. Section V gives a summary of the paper.

Throughout the paper, we adopt geometric units with $c = G = 1$, where c and G denote the speed of light and the gravitational constant respectively. We adopt $(-, +, +, +)$ for the metric signature.

II. FORMALISM

A. The Two-fluid Model and Equation of State

We briefly review the derivation of the two-fluid Tolman–Oppenheimer–Volkoff (TOV) equations [48–50]. The Einstein field equation reads

$$G^{\mu\nu} = 8\pi T^{\mu\nu}, \quad (1)$$

where $G^{\mu\nu}$ and $T^{\mu\nu}$ are the Einstein tensor and energy-momentum tensor of matters, respectively. Considering the results of underground DM search experiments [14–17], strict

constraints were set for the DM-BM coupling strength [51]. For this reason, to the leading order we neglect all interactions between DM and BM except gravity. So the energy-momentum tensor can be divided into the BM component, $T_{\text{BM}}^{\mu\nu}$, and DM component, $T_{\text{DM}}^{\mu\nu}$,

$$T^{\mu\nu} = T_{\text{BM}}^{\mu\nu} + T_{\text{DM}}^{\mu\nu}. \quad (2)$$

Each of them is conserved,

$$T_{\text{BM};\nu}^{\mu\nu} = T_{\text{DM};\nu}^{\mu\nu} = 0. \quad (3)$$

The two energy-momentum tensors are written as

$$T_{\text{BM}}^{\mu\nu} = (\epsilon_{\text{BM}} + p_{\text{BM}})u_{\text{BM}}^{\mu}u_{\text{BM}}^{\nu} + p_{\text{BM}}g^{\mu\nu}, \quad (4)$$

$$T_{\text{DM}}^{\mu\nu} = (\epsilon_{\text{DM}} + p_{\text{DM}})u_{\text{DM}}^{\mu}u_{\text{DM}}^{\nu} + p_{\text{DM}}g^{\mu\nu}. \quad (5)$$

Taking the spherical symmetry, we can write the spacetime line element as $ds^2 = -e^{2\mu}dt^2 + e^{2\nu}dr^2 + r^2(d\theta^2 + \sin^2\theta d\phi^2)$, where μ and ν are functions of r . From Eq. (1) and (3), the two-fluid TOV equations can be derived as

$$\frac{dm_i}{dr} = 4\pi r^2 \epsilon_i, \quad (6)$$

$$\frac{dp_i}{dr} = -\frac{4\pi r^3 p + m}{r^2(1 - 2m/r)}(\epsilon_i + p_i), \quad (7)$$

where the subscripted i denotes the fluid (DM or BM), $p = p_{\text{DM}} + p_{\text{BM}}$, and $m = m_{\text{DM}} + m_{\text{BM}}$. The particle number of each component N_i is

$$\frac{dN_i}{dr} = \frac{4\pi r^2 n_i}{\sqrt{1 - 2m/r}}, \quad (8)$$

where n_i is the particle number density.

We use the asymmetric fermionic DM model as a prototype, which is often approximately regarded as a free Fermi gas at zero temperature. From thermodynamic statistics, the energy density, pressure, and number density are [52]

$$\epsilon = \frac{1}{2\pi^2} \int_0^{k_F} k^2 \sqrt{k^2 + m_f^2} dk = \frac{1}{8\pi^2} \left[k_F \sqrt{m_f^2 + k_F^2} (2k_F^2 + m_f^2) - m_f^4 \ln \left(\frac{k_F + \sqrt{m_f^2 + k_F^2}}{m_f} \right) \right], \quad (9)$$

$$p = \frac{1}{6\pi^2} \int_0^{k_F} \frac{k^4}{\sqrt{k^2 + m_f^2}} dk = \frac{1}{24\pi^2} \left[k_F \sqrt{m_f^2 + k_F^2} (2k_F^2 - 3m_f^2) + 3m_f^4 \ln \left(\frac{k_F + \sqrt{m_f^2 + k_F^2}}{m_f} \right) \right], \quad (10)$$

$$n = \frac{k_F^3}{3\pi^2}, \quad (11)$$

where k_F is the Fermi momentum. Considering these formulas and eliminating k_F , we obtain $p(\epsilon)$. The EOS of bosonic DM can be found in Eq. (17) at the end of Section IV. For the EOS of BM, we use AP4 model for illustration [53]. With

this setting, we can obtain the structure of DANSs and the surrounding spacetime via integration of the two-fluid TOV equations.

B. The Critical Curve

An important question is whether a DANS is stable under perturbations. In the case of pure NSs, each solution of the TOV equation is uniquely identified by a single quantity, the central pressure. The entire star becomes unstable if its central pressure exceeds the critical point that corresponds to the maximum mass [52]. However, when it comes to two-fluid systems, there are *two* kinds of fluids and *two* independent central pressures. One is the central pressure of DM, p_{DM}^c , and the other is the central pressure of BM, p_{BM}^c . Thus there is a critical curve instead of a critical point in the p_{BM}^c - p_{DM}^c plane.

The way to get the critical curve is not simply searching for the maximum mass while fixing one central pressure and varying the other. The radical oscillation of a DANS under small perturbations is a problem of the Sturm-Liouville type, with eigenvalues $\omega_0^2 < \omega_1^2 < \omega_2^2 < \dots$, where ω_0 is the eigenfrequency of the fundamental mode. The critical points with $\omega = 0$ mark the onset of instability [52, 54]. Because N_{DM} and N_{BM} conserve in perturbations, Henriques *et al.* [55] proposed an equivalent yet more straightforward criterion,

$$\frac{dM}{dp} = \frac{dN_{\text{DM}}}{dp} = \frac{dN_{\text{BM}}}{dp} = 0, \quad (12)$$

where M is the total mass, and \mathbf{p} is a vector that is simultaneously tangent to both N_i contour lines in the central pressure parameter space. Jetzer [56] has proved that dM can be written as a linear combination of two dN_i at these points. So $dM/d\mathbf{p} = 0$ holds naturally if $dN_i/d\mathbf{p} = 0$.

Using this criterion, we adopt the methods used by Kain [11] to compute the critical curve. This involves computing contour lines of N_{DM} in the central pressure parameter space using Eq. (8) and Eq. (11). Once the contour lines are determined, we follow one line to search for the point where M reaches its maximum. The critical curve then consists of all these points.

III. STRUCTURE OF DARK-MATTER-ADMIXED NEUTRON STARS

By choosing a pair of central pressures as the initial value, we can solve the two-fluid TOV equations. The pressures will decrease from the center to the surfaces at R_i , which are defined by $p_i = 0$. If R_{DM} is less than R_{BM} , the DANS has a DM core. Conversely, it has a DM halo. Figure 1 shows the p_{BM}^c - p_{DM}^c parameter space of DANSs for $m_f = 0.5$ GeV. The critical curve is drawn with a thick black line. The parameter space below the critical curve gives stable static solutions. The orange area indicates static solutions with a DM halo, while the blue area indicates those with a DM core.

In the one-fluid system, a 1-dimensional central pressure parameter space results in a mass-radius curve. Accordingly, a 2-dimensional p_{BM}^c - p_{DM}^c parameter space results in a 2-dimensional M - R_{BM} diagram in the two-fluid system. Here M and R_{BM} are the most essential and straightforward observables. In Fig. 2, we show the relation between M and R_{BM}

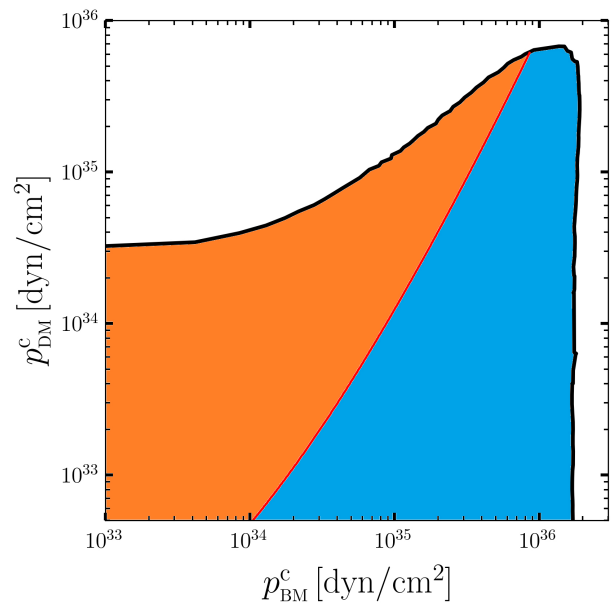


FIG. 1. The p_{BM}^c - p_{DM}^c parameter space for solutions in the two-fluid model with $m_f = 0.5$ GeV.

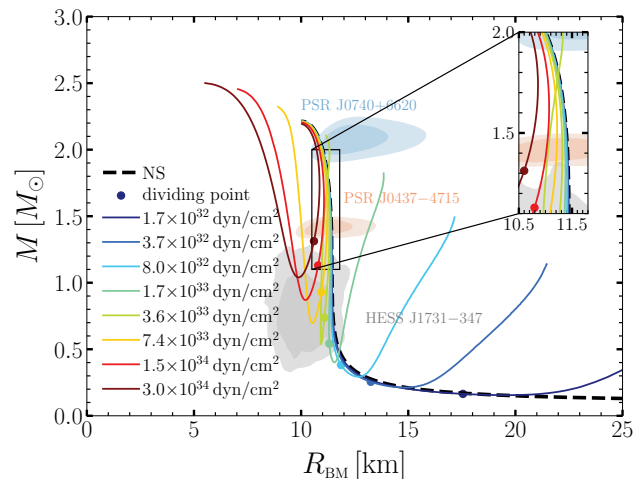


FIG. 2. The M - R_{BM} relations of DANSs for $m_f = 0.5$ GeV, with different colors indicating different p_{DM}^c . NICER constraints are included for PSRs J0740+6620 [40, 57, 58] (blue regions), J0437-4715 [59, 60] (orange regions), and HESS J1731-347 [61] (grey regions). Contours show 68.3% and 95.4% credible intervals.

for $m_f = 0.5$ GeV. The thick black dashed line is the mass-radius curve for pure NSs, and lines with different colors show DANSs. Each line maintains a constant p_{DM}^c while changing p_{BM}^c . Meanwhile, the solid dots are dividing points between solutions with a DM halo and a DM core. Points closer to the dashed line are solutions with a DM core, while the other corresponds to solutions with a DM halo. When p_{BM}^c gets large enough, a DANS has a DM core, and the lines in the figure get closer to the thick black dashed line. That means a DM core affects the structure of DANSs slightly, just making M and

R_{BM} a little smaller compared to the NSs with the same p_{BM}^{c} . When p_{BM}^{c} is small, a DANS has a DM halo and a significantly different structure. For a pure NS, a smaller p_{BM}^{c} will result in a larger radius and a smaller mass. However, the existence of DM will increase the total mass, and make the BM core shrink further due to the gravity of DM. That is also why R_{BM} tends to decrease while M tends to increase as p_{DM}^{c} increases. In addition, different central pressures can result in a same set of M and R_{BM} , as the lines intersecting with each other in Fig. 2.

When $m_f = 0.5 \text{ GeV}$, DANSs with either a DM core or a DM halo can be generated while their masses remain near $1 M_{\odot}$. Two further examples with different m_f are given in Fig. 3. When m_f is smaller, the DM halo scenario (solutions with a DM halo) occurs near the dashed line and then move upwards. That is because that diffuse DM is easier to form a DM halo and allow more DM to exist. When m_f is larger, the DM halo scenario will be compressed at the bottom.

IV. MODIFICATION OF PULSE PROFILES BY DARK MATTER HALOS

A. Light Bending Effects of Gravitational Fields

In this subsection, we briefly outline the methods to calculate the X-ray pulsar pulse profile. For detailed derivation, readers can refer to Silva and Yunes [62] and Xu *et al.* [63]. We assume there is a pair of hot spots on the BM surface of a DANS with a DM halo. The radiation from each of these point-like emitting regions is presumed to be isotropic [64]. Light emitted from them will be subject to additional light bending effects due to the gravity of the DM halo. In the presence of DM, the metric of spacetime outside the BM core is no longer the Schwarzschild metric, though it is still spherical symmetric [65].

Following Refs. [43, 62, 63], we introduce some geometry quantities (see Fig. 8 in Ref. [63]) and the calculation of the flux for arbitrary spherically symmetric metric. In the model, a pair of hot spots is located on the BM surface with colatitudes of γ and $\pi - \gamma$ measured from the spin axis; \mathbf{n} is a unit vector pointing to one hot spot from the center of the star; \mathbf{k}_0 is a unit vector in the direction of light emission; \mathbf{k} is a unit vector in the direction of light after bending; β stands for the velocity of the emitting region in the local static frame. There are four other relevant angles: the angle ι between the line of sight and the spin axis, the angle ψ between the line of sight and \mathbf{n} , the angle α between \mathbf{k}_0 and \mathbf{n} , and the angle ζ between \mathbf{k}_0 and β [63].

The observed differential flux in terms of the quantities at the emitting region is [66]

$$dF = \delta^5 g(R_{\text{BM}}) I'(v') dv' \frac{\cos \alpha \sin \alpha}{\sin \psi} \frac{d\alpha}{d\psi} \frac{dS'}{D^2}, \quad (13)$$

where δ is the Doppler factor, $I'(v')$ is the radiation intensity as a function of frequency in the comoving frame, dS' is the proper differential area at the emitting region, D is the distance between the pulsar and the observer, and we have defined $-g$ as the t - t component of the metric. The

Doppler factor, describing how the boost speed β caused by the pulsar rotation affects the flux, can be written as $\delta = \sqrt{1 - \beta^2} / (1 - \beta \cos \zeta)$ [67].

Through the analysis in the local static frame [66], we can calculate β and $\cos \zeta$ by $\beta = R_{\text{BM}} \Omega \sin \gamma / \sqrt{g(R_{\text{BM}})}$ and $\cos \zeta = -\sin \alpha \sin \iota \sin(\Omega t_0) / \sin \psi$, where Ω is the angular velocity of pulsar rotation, and t_0 is the coordinate time when the ray is emitted and has been set to zero when the spot is the closest to the observer. The relation between ψ and α can be derived by doing an integral along the path of light propagation [68], $\psi = \int_{R_{\text{BM}}}^{\infty} \sqrt{f g} [r^{-2} \sigma^{-2} - r^{-4} g] dr$, where f is the r - r component of the metric and $\sigma \equiv R_{\text{BM}} \sin \alpha / \sqrt{g(R_{\text{BM}})}$ is the impact parameter.

The flux is normalized by a factor $\int I'(v') dv' dS' / D^2$,

$$F \equiv \frac{D^2 \int dF}{dS' \int I'(v') dv'} = \delta^5 g(R_{\text{BM}}) \frac{\cos \alpha \sin \alpha}{\sin \psi} \frac{d\alpha}{d\psi}. \quad (14)$$

Using geometric analysis, we obtain $\cos \psi = \cos \iota \cos \gamma + \sin \iota \sin \gamma \sin(\Omega t_0)$. Thus every emission time t_0 corresponds to an angle ψ , an impact parameter σ , and an emission angle α . Then we calculate the observer time, t_{obs} , which is different from t_0 because the time of light propagation differs. Taking this time delay into consideration, we finally obtained [68],

$$t_{\text{obs}} = t_0 + \int_{R_{\text{BM}}}^{\infty} \sqrt{\frac{f}{g}} \left[\left(1 - \frac{\sigma^2 g}{r^2} \right)^{-\frac{1}{2}} - 1 \right] dr. \quad (15)$$

Eventually, using Eq. (14) and Eq. (15), we obtain the relation between the normalized flux and the observer time, namely the pulse profile.

B. X-Ray Pulse Profile Flux

Previously, Miao *et al.* [45] studied the pulse profiles of DANSs, fixing the BM core radius, R_{BM} , and the core mass, $M(R_{\text{BM}})$. To characterize the effects of DM, they defined a quantity, $M_{\text{halo}}/R_{\text{DM}}$, where $M_{\text{halo}} = M - M(R_{\text{BM}})$, is the mass of the DM halo. In fact, it is the half of the increase of the t - t component of the metric, $g(R_{\text{DM}})$, when adding a halo. Here g plays an important role in calculating the flux intensity. In our study, as mentioned in Sec. I, we assume that M and R_{BM} are potential observables, respectively from orbital dynamics and X-ray emission modeling. In this scenario, we find that the flux deviation—with respect to a normal NS—is better dependent on $M_{\text{halo}}/R_{\text{BM}}$ than $M_{\text{halo}}/R_{\text{DM}}$. So we choose $M_{\text{halo}}/R_{\text{BM}}$ as a characteristic quantity in describing the effects of DM halos on pulse profiles. In Table I we choose $m_f = 0.5 \text{ GeV}$ for illustration, and show two pairs of DANSs (DANS1 and DANS2) and normal NSs with the same M and R_{BM} . DANS1 and DANS2 have similar M and R_{BM} , but DANS1 has a lighter DM halo than DANS2.

In the upper panel of Fig. 4, we show the pulse profiles from point-like hot spots with $\gamma = 45^\circ$ and $\iota = 45^\circ$, from a pulsar with a rotational period $T = 5 \text{ ms}$. The normalized flux deviation, $\Delta F/F \equiv (F_{\text{DANS}} - F_{\text{NS}})/F_{\text{NS}}$, as a function of t_{obs} , is

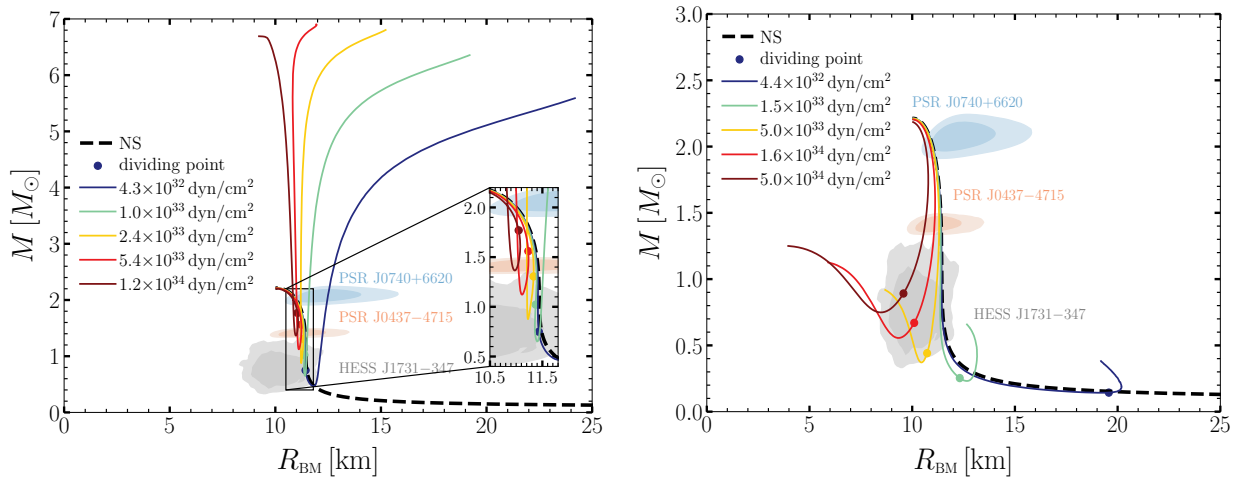


FIG. 3. The M - R_{BM} relations of DANSSs. The left panel is for $m_f = 0.3$ GeV, showing the DM halo region near the dashed line and above. The right panel is for $m_f = 0.7$ GeV, showing the DM halo region compressed at the bottom.

TABLE I. Relevant parameters of two DANSSs and corresponding normal NSs, whose M and R_{BM} are the same. The DM particle mass m_f is fixed to 0.5 GeV.

Model	R_{BM}/km	R_{DM}/km	M/M_{\odot}	M_{DM}/M_{\odot}	$M_{\text{halo}}/M_{\odot}$	$M_{\text{halo}}/R_{\text{BM}}$
DANS1	9.5	16.9	1.2	0.44	0.11	0.016
NS1	9.5	—	1.2	0	0	0
DANS2	11.5	51.5	1.4	1.27	1.14	0.146
NS2	11.5	—	1.4	0	0	0

shown in the lower panel of the figure, where F_{DANS} and F_{NS} are respectively fluxes of DANSSs and normal NSs. As shown in this figure, the fraction $M_{\text{halo}}/R_{\text{BM}}$ significantly affects the DANSS pulse profiles. The maximum deviation occurs near the peak of the pulse profile. Compared to a normal NS, DANSS pulse flux tends to exhibit increased brightness during high-luminosity periods, and decreased brightness during low-luminosity periods. That can be explained by Eq. (14). F and $g(R_{\text{BM}})$ are positively correlated. For DANSSs, $g(R_{\text{BM}})$ is larger because of the existence of DM halos. As a result, F_{DANS} will fluctuate in a wider range. It always holds true for large $M_{\text{halo}}/R_{\text{BM}}$ since the difference of $g(R_{\text{BM}})$ between DANSSs and NSs is big enough. However, it is not shown in this figure that when $M_{\text{halo}}/R_{\text{BM}}$ drops to about 10^{-4} , the amplitude of F_{DANS} may become less than F_{NS} .

More realistically, we extend our study to a scenario where the emitting regions are extended. We assume their diameters to be $d = 3$ km. We consider a grid of emission spots on the surface [43, 69]. We use the same values for γ and ι , namely $\gamma = 45^\circ$ and $\iota = 45^\circ$. To show the differences between point-like emitting regions and extended emitting regions, we plot a comparison of pulse profiles from DANSS1 in Fig. 5. An obvious feature of the curve representing the extended emitting region is the absence of sharp turns. The sharp turn in the point-like case comes from the emitting region with a colatitude $\gamma = 135^\circ$ (the opposite patch). This region remains invisible when it turns away from the line of sight. It only contributes to the overall flux during a part of the rotational

period. Considering an extended emitting region as an ensemble of point-like sources, each of them has a distinct sharp turn. The addition of them gives a smooth pulse profile.

To see the effect from DM halos, taking DANSS1 and NS1 as example, the pulse profiles from extended emitting regions are shown in Fig. 6. The upper panel is their pulse profiles, and the lower panel is $\Delta F/F$. Our previously derived conclusions based on point-like emitting regions remain qualitatively applicable here. Compared with the point-like case, the pulse profile from the extended emitting region exhibits a smaller range between its minimum and maximum fluxes. The difference is about 20% in Fig. 5. To provide an explanation, we investigate the impact of the colatitude of the emitting region, γ , and the observer's relative position, represented by ι . To see the deviation more clearly, we take the example of DANSS2 and NS2. The modification of the peak flux with different γ and ι are shown in Fig. 7. These two angles exhibit similar impacts on the pulse profile, as they always appear in pair in the formulas except for the Doppler factor, which is relatively small. When $\gamma = \iota$, the most significant deviation of the pulse profile occurs. However, in the context of extended emitting regions, $\gamma = \iota$ does not hold at each point. As a result, the final pulse profile exhibits a gentler overall behavior.

To provide a comprehensive overview of how DM halos affect pulse profiles, we compute the peak flux deviations for different central pressures for $m_f = 0.5$ GeV, assuming the presence of a DM halo. We only consider DANSSs with $R_{\text{BM}} > 3M$, which is a reasonable assumption considering the

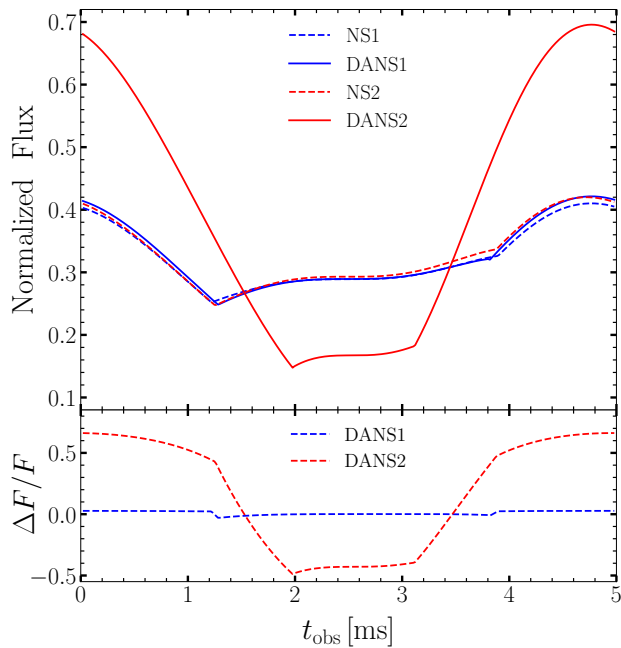


FIG. 4. (Upper) Pulse profiles from two point-like hot spots of the DANSs and NSs in Table I. The emitting region in the northern hemisphere is located at a colatitude $\gamma = 45^\circ$. The inclination angle of the line of sight is $\iota = 45^\circ$. (Lower) Deviation of DANS pulse profiles with respect to the corresponding normal NS pulse profiles.

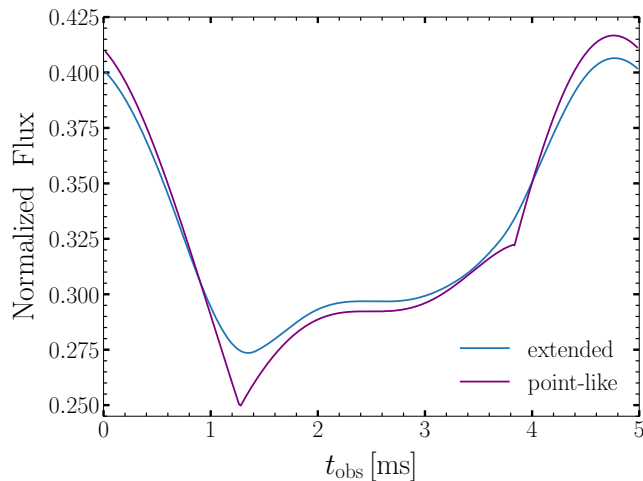


FIG. 5. Comparison of pulse profiles of DANS1 with point-like and extended emitting regions.

constraints on the EOS [68]. Our results are depicted in Fig. 8, revealing the substantial influence of DM halos across most parameter space for DM halos. When the central pressures lie near the dividing line between the DM halo and the DM core (see Fig. 1), their pulse profiles exhibit minimal deviation. Overall, as expected, the peak flux deviation tends to increase with an increasing p_{DM}^c when p_{BM}^c is fixed.

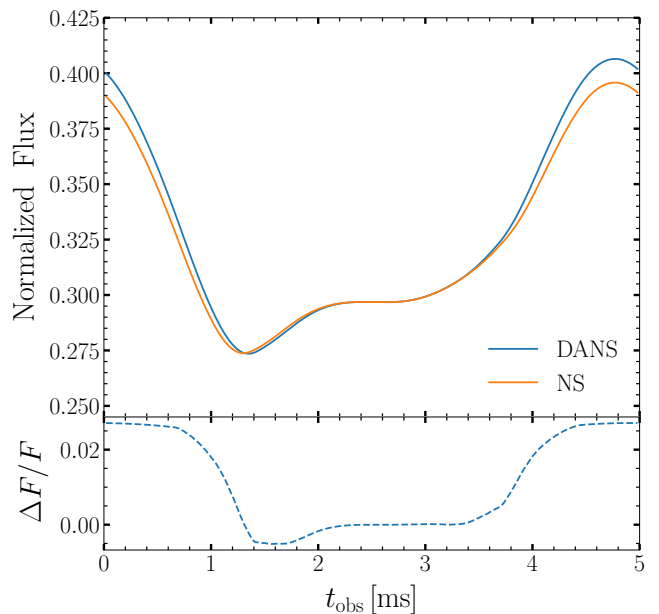


FIG. 6. Pulse profiles of DANS1 and NS1 (see Table I) with a pair of the emitting region, γ , and the inclination angle of the line of sight, ι .

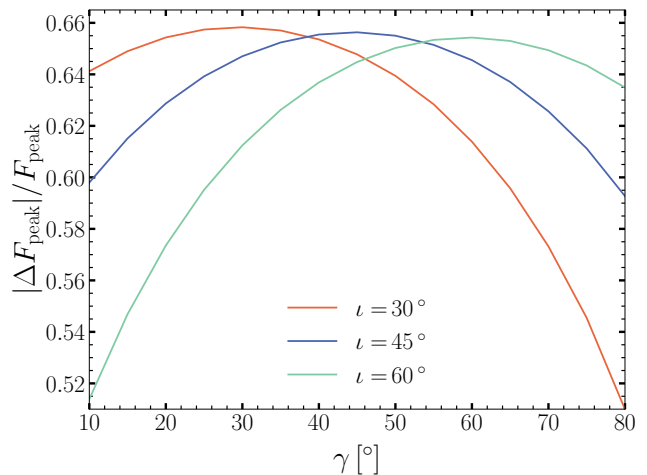


FIG. 7. Influence of the colatitude γ and the inclination ι to the peak flux deviation of the emitting region between DANS2 and NS2.

C. Universal Relations

The impacts of central pressures on peak flux deviations have been shown in Fig. 8. However, we want to derive a more direct relation. As mentioned above, the deviation might be highly dependent on the quantity $M_{\text{halo}}/R_{\text{BM}}$. To verify this hypothesis, we calculate a series of flux deviations systematically with a varying m_f . For each m_f , we randomly select M and R_{BM} from the M - R_{BM} diagram where DANSs have halos. Existing observations have already established constraints on the mass and radius of NSs [57, 70–72]. To remain within these bounds, we only consider cases where $M \in [1, 3] M_\odot$ and $R_{\text{BM}} \in [8, 20]$ km. The colatitude of the northern point-

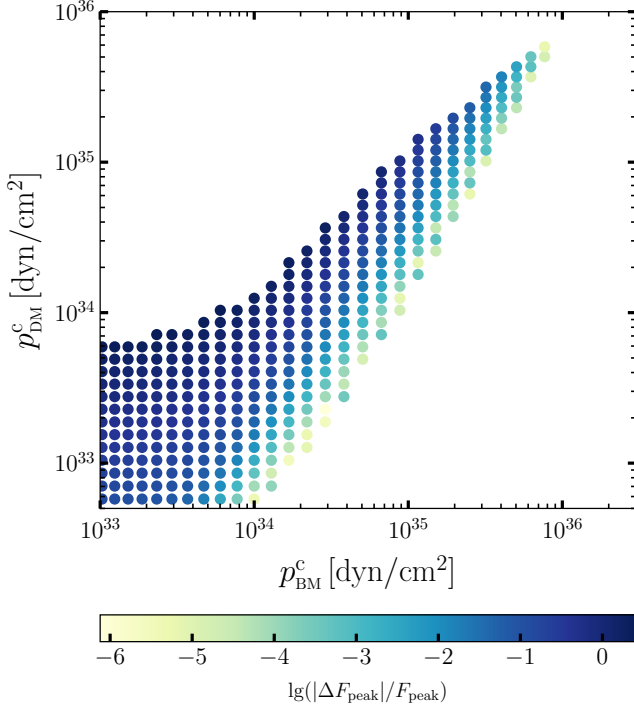


FIG. 8. Peak flux deviation in the p_{DM}^c - p_{DM}^c parameter space for $m_f = 0.5$ GeV. Here all DANs have a DM halo. The area with the smallest deviation is near the dividing line between the DM halo and the DM core (see Fig. 1).

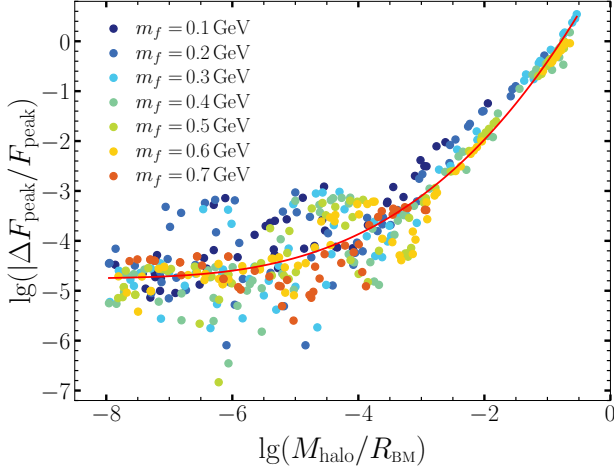


FIG. 9. Peak flux deviation as a function of $M_{\text{halo}}/R_{\text{BM}}$. Each point is a randomly chosen DANs. Different colors represent different m_f . The solid line is a fitted curve given by Eq. (16).

like emitting region γ and the inclination angle ι are randomly distributed in $[30^\circ, 60^\circ]$.

In Fig. 9, we show $|\Delta F_{\text{peak}}|/F_{\text{peak}}$ against $M_{\text{halo}}/R_{\text{BM}}$ using logarithmic scales. Over a range of $m_f \in [0.1, 0.7]$ GeV, $M_{\text{halo}}/R_{\text{BM}} \in [1.1 \times 10^{-8}, 2.9 \times 10^{-1}]$, all of the randomly selected data points can be loosely fitted by a cubic function. Defining $f_F(x) = \lg(|\Delta F_{\text{peak}}|/F_{\text{peak}})$, $x = \lg(M_{\text{halo}}/R_{\text{BM}})$, the

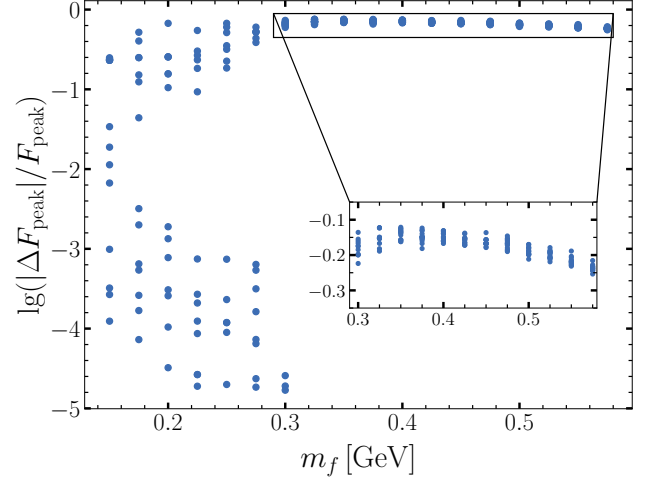


FIG. 10. Peak flux deviation versus the DM particle mass. There are two branches of solutions in the figure: one spans all m_f in the figure, while the other stops at $m_f = 0.3$ GeV.

universal relation is represented by the following formula,

$$f_F(x) = 0.012x^3 + 0.290x^2 + 2.351x + 1.667. \quad (16)$$

In particular, the maximum deviation of the peak flux exceeds 100% when $M_{\text{halo}}/R_{\text{BM}} = 0.292$ and $m_f = 0.3$ GeV, which can potentially lead to a significant impact on observations. Take PSR J0740+6620 as an example [40, 57, 58]. A good constraint on the mass and radius was obtained using about three years' NICER data, with the total net exposure time about 10^6 sec. The uncertainty of the telescope was estimated to be about 10%, that means the flux variations might be observable. Analyzing X-ray pulses of DANs represents a theoretically viable approach to searching for DM.

We investigate how DM halos affect pulsar pulse profiles of DANs with typical NS masses and radii. For a normal NS with a mass of $1.4 M_\odot$, the AP4 EOS yields a radius of 11.4 km. We randomly choose DANs with $M \in [1.37, 1.43] M_\odot$ and $R_{\text{BM}} \in [11.2, 11.6]$ km. The peak flux deviation versus the DM particle mass m_f is shown in Fig. 10. When $m_f > 0.3$ GeV, the peak flux deviation remains nearly constant at about 70%. To enhance clarity, we include a smaller inset figure that magnifies this region. When $m_f < 0.3$ GeV, the data points are largely scattered.

It is clear that there are two branches of solutions in Fig. 10. One of the branches spans all m_f in the figure, while the other stops at $m_f = 0.3$ GeV. To provide an explanation, we define a “solution region” where $M \in [1.37, 1.43] M_\odot$ and $R_{\text{BM}} \in [11.2, 11.6]$ km. Following Figs. 2–3, for heavy DM particles, say, $m_f = 0.7$ GeV, the parameter space for DM halo would not overlap with the solution region. When m_f is smaller, the data points for DM halos move upwards, overlapping with the solution region. When m_f continues to decrease, the dividing points get closer to the black dashed lines (see Figs. 2–3), and the second branch of solution occurs. These solutions are near the dividing points, which means a much more diffuse DM halo, resulting in a smaller flux deviation.

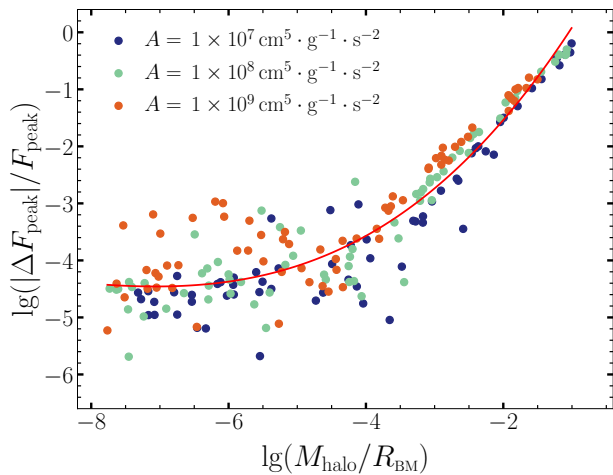


FIG. 11. Peak flux deviation as a function of $M_{\text{halo}}/R_{\text{BM}}$ for bosonic DM. Different colors are for different A in Eq. (17). The solid line gives the universal relation in Eq. (18).

The closer the solution is to the dividing points, the smaller the flux deviation is. When m_f is small, the effect of a diffuse DM halo is insignificant. For example, when $M_{\text{halo}}/R_{\text{BM}} \sim 10^{-2}$ or 10^{-6} , according to Fig. 9, the quantity $|\Delta F_{\text{peak}}|/F_{\text{peak}}$ may differ within $[10^{-5}, 10^{-2}]$. However, for a larger m_f , there is no DANS with a diffuse DM halo in the solution region. The quantity $|\Delta F_{\text{peak}}|/F_{\text{peak}}$ remains in $[10^{-0.3}, 10^{-0.1}]$. Consequently, the peak flux deviation induced by a heavy DM mass can exceed the one induced by a light DM mass by orders of magnitude, due to significantly different DANS central pressures. These two varied scenarios manifest as either diffusion of data points for a small m_f or clustering of data points for a large m_f when plotted on a logarithmic scale.

Bosonic DM is another candidate in explaining the DM phenomenology. In a simple model, the EOS of bosonic DM can be written as [73, 74]

$$p = A\rho^2, \quad (17)$$

where $A = 2\pi l/m_f^3$ with l the scattering length. The universal relation between $\lg(|\Delta F_{\text{peak}}|/F_{\text{peak}})$ and $\lg(M_{\text{halo}}/R_{\text{BM}})$ for bosonic DM halos is shown in Fig. 11. In particular, as shown by the solid line in the figure, the universal relation can be loosely represented by the following formula,

$$f_B(x) = 0.010x^3 + 0.270x^2 + 2.364x + 2.190, \quad (18)$$

where $f_B(x) = \lg(|\Delta F_{\text{peak}}|/F_{\text{peak}})$, and $x = \lg(M_{\text{halo}}/R_{\text{BM}})$.

We derive two universal relations concerning fermionic DM and bosonic DM, respectively given in Eq. (16) and Eq. (18); also see Fig. 9 and Fig. 11. Striking similarities can be seen, which underscores the generality of our results.

V. CONCLUSIONS

In our study, we analyzed the structure of DANSs in a two-fluid model. Different M - R_{BM} diagrams for DANSs were constructed considering different DM particle mass, m_f . Via integration of the TOV equations, a DANS possesses either a DM core or a DM halo. Our primary focus lies in investigating the impact of DM halos on X-ray pulsar pulse profiles. The pulse profiles of DANSs were compared with those of normal NSs. In contrast to earlier studies, we fixed the total mass M , instead of the core mass $M(R_{\text{BM}})$, considering that M is a more fundamental and direct observable. Similarly, we also fixed the BM core radius, R_{BM} .

Our calculations revealed that the presence of dense DM halos will increase the amplitude of X-ray flux fluctuation. Besides examining point-like hot spots, we explored the effects of extended emitting regions. We found that extended emitting regions tend to reduce the gap between the minimum and maximum fluxes, by about 20% (see Fig. 5). The impacts of the position of emitting regions, represented by the colatitude angle γ , and the inclination angle to the line of sight, ι , were also studied. The influences of γ and ι on the pulse profiles are similar. When $\gamma = \iota$, the influence reaches its maximum.

Furthermore, we observed a universal correlation between the peak flux deviation of DANSs with respect to normal NSs, and the dimensionless quantity, $M_{\text{halo}}/R_{\text{BM}}$. Remarkably, this relation remains consistent when considering both fermionic and bosonic DM models. In this paper, we did not consider self-interacting DM, which is a very interesting topic in DM studies (see e.g. Ref. [75]). However, focusing on the universal relation, Miao *et al.* [45] have studied fermionic self-interacting DM via a repulsive Yukawa type, and the relation of theirs holds when the interaction strength is randomly chosen. In-depth studies concerning different interactions and rich phenomena are left to future investigation. We also studied DANSs with typical masses and radii ($M \simeq 1.4 M_{\odot}$ and $R_{\text{BM}} \simeq 11.4$ km). It is interesting that the peak flux deviation can be divided into two different branches, in which the larger deviation stays at about 70%. In all calculated examples, the maximum deviation of the pulse profiles can exceed 100% when $M_{\text{halo}}/R_{\text{BM}} = 0.292$ and $m_f = 0.3$ GeV, leading to a potentially significant observable difference. Our study suggests that X-ray observation of pulsars may be a feasible way to search for DM.

ACKNOWLEDGMENTS

This work was supported by the Beijing Natural Science Foundation (QY23009, 1242018), the National SKA Program of China (2020SKA0120300), the National Natural Science Foundation of China (11991053), the Max Planck Partner Group Program funded by the Max Planck Society, and the High-Performance Computing Platform of Peking University.

- [1] P. Mocz *et al.*, *Phys. Rev. Lett.* **123**, 141301 (2019), arXiv:1910.01653 [astro-ph.GA].
- [2] Y. Sofue and V. Rubin, *Ann. Rev. Astron. Astrophys.* **39**, 137 (2001), arXiv:astro-ph/0010594.
- [3] R. Fadely and C. R. Keeton, *Mon. Not. Roy. Astron. Soc.* **419**, 936 (2012), arXiv:1109.0548 [astro-ph.CO].
- [4] N. Aghanim *et al.* (Planck), *Astron. Astrophys.* **641**, A6 (2020), [Erratum: *Astron. Astrophys.* 652, C4 (2021)], arXiv:1807.06209 [astro-ph.CO].
- [5] L. Shao and K. Yagi, *Sci. Bull.* **67**, 1946 (2022), arXiv:2209.03351 [gr-qc].
- [6] G. Bertone and M. Fairbairn, *Phys. Rev. D* **77**, 043515 (2008), arXiv:0709.1485 [astro-ph].
- [7] C. Kouvaris and P. Tinyakov, *Phys. Rev. D* **82**, 063531 (2010), arXiv:1004.0586 [astro-ph.GA].
- [8] S. C. Leung, M. C. Chu, and L. M. Lin, *Phys. Rev. D* **84**, 107301 (2011), arXiv:1111.1787 [astro-ph.CO].
- [9] Q.-F. Xiang, W.-Z. Jiang, D.-R. Zhang, and R.-Y. Yang, *Phys. Rev. C* **89**, 025803 (2014), arXiv:1305.7354 [astro-ph.SR].
- [10] J. Ellis, G. Hütsi, K. Kannike, L. Marzola, M. Raidal, and V. Vaskonen, *Phys. Rev. D* **97**, 123007 (2018), arXiv:1804.01418 [astro-ph.CO].
- [11] B. Kain, *Phys. Rev. D* **103**, 043009 (2021), arXiv:2102.08257 [gr-qc].
- [12] Y. Wang, X. Miao, and L. Shao, *Acta Astron. Sin.* **62**, 97 (2021).
- [13] M. Hippert, E. Dillingham, H. Tan, D. Curtin, J. Noronha-Hostler, and N. Yunes, *Phys. Rev. D* **107**, 115028 (2023), arXiv:2211.08590 [astro-ph.HE].
- [14] D. S. Akerib *et al.* (LUX), *Phys. Rev. Lett.* **118**, 021303 (2017), arXiv:1608.07648 [astro-ph.CO].
- [15] E. Aprile *et al.* (XENON), *Phys. Rev. Lett.* **121**, 111302 (2018), arXiv:1805.12562 [astro-ph.CO].
- [16] Y. Meng *et al.* (PandaX-4T), *Phys. Rev. Lett.* **127**, 261802 (2021), arXiv:2107.13438 [hep-ex].
- [17] J. Aalbers *et al.* (LZ), *Phys. Rev. Lett.* **131**, 041002 (2023), arXiv:2207.03764 [hep-ph].
- [18] D. Singh, A. Gupta, E. Berti, S. Reddy, and B. S. Sathyaprakash, *Phys. Rev. D* **107**, 083037 (2023), arXiv:2210.15739 [gr-qc].
- [19] D. Liang and L. Shao, *JCAP* **08**, 016 (2023), arXiv:2303.05107 [astro-ph.HE].
- [20] G. L. Comer, D. Langlois, and L. M. Lin, *Phys. Rev. D* **60**, 104025 (1999), arXiv:gr-qc/9908040.
- [21] D. Noordhuis, A. Prabhu, S. J. Witte, A. Y. Chen, F. Cruz, and C. Weniger, *Phys. Rev. Lett.* **131**, 111004 (2023), arXiv:2209.09917 [hep-ph].
- [22] M. Cernieño, M. A. Pérez-García, and J. Silk, *Publ. Astron. Soc. Austral.* **34**, e043 (2017), arXiv:1710.06866 [astro-ph.HE].
- [23] D. Blas, D. L. Nacir, and S. Sibiryakov, *Phys. Rev. Lett.* **118**, 261102 (2017), arXiv:1612.06789 [hep-ph].
- [24] T. Malik, B. K. Agrawal, J. N. De, S. K. Samaddar, C. Providência, C. Mondal, and T. K. Jha, *Phys. Rev. C* **99**, 052801 (2019), arXiv:1901.04371 [nucl-th].
- [25] P. Pani, *Phys. Rev. D* **92**, 123530 (2015), arXiv:1512.01236 [astro-ph.HE].
- [26] S. J. Witte, D. Noordhuis, T. D. P. Edwards, and C. Weniger, *Phys. Rev. D* **104**, 103030 (2021), arXiv:2104.07670 [hep-ph].
- [27] A. Hook, Y. Kahn, B. R. Safdi, and Z. Sun, *Phys. Rev. Lett.* **121**, 241102 (2018), arXiv:1804.03145 [hep-ph].
- [28] B. R. Safdi, Z. Sun, and A. Y. Chen, *Phys. Rev. D* **99**, 123021 (2019), arXiv:1811.01020 [astro-ph.CO].
- [29] A. de Lavallaz and M. Fairbairn, *Phys. Rev. D* **81**, 123521 (2010), arXiv:1004.0629 [astro-ph.GA].
- [30] C. Kouvaris, *Phys. Rev. D* **77**, 023006 (2008), arXiv:0708.2362 [astro-ph].
- [31] D. R. Karkevandi, S. Shakeri, V. Sagun, and O. Ivanytskyi, *Phys. Rev. D* **105**, 023001 (2022), arXiv:2109.03801 [astro-ph.HE].
- [32] S. Shakeri and D. R. Karkevandi, *Phys. Rev. D* **109**, 043029 (2024), arXiv:2210.17308 [astro-ph.HE].
- [33] R. F. Dieckrichs, N. Becker, C. Jockel, J.-E. Christian, L. Sagunski, and J. Schaffner-Bielich, *Phys. Rev. D* **108**, 064009 (2023), arXiv:2303.04089 [gr-qc].
- [34] M. Deliyergiyev, A. Del Popolo, and M. L. Delliou, *Mon. Not. Roy. Astron. Soc.* **527**, 4483 (2023), arXiv:2311.00113 [astro-ph.GA].
- [35] P. Thakur, T. Malik, and T. K. Jha, *Particles* **7**, 80 (2024), arXiv:2401.07773 [hep-ph].
- [36] S. I. Blinnikov and M. Khlopov, *Sov. Astron.* **27**, 371 (1983).
- [37] M. Y. Khlopov, G. M. Beskin, N. E. Bochkarev, L. A. Pustyl'nik, and S. A. Pustyl'nik, *Sov. Astron.* **35**, 21 (1991).
- [38] T. E. Riley *et al.*, *Astrophys. J. Lett.* **887**, L21 (2019), arXiv:1912.05702 [astro-ph.HE].
- [39] M. C. Miller *et al.*, *Astrophys. J. Lett.* **887**, L24 (2019), arXiv:1912.05705 [astro-ph.HE].
- [40] M. C. Miller *et al.*, *Astrophys. J. Lett.* **918**, L28 (2021), arXiv:2105.06979 [astro-ph.HE].
- [41] S. Vinciguerra *et al.*, *Astrophys. J.* **961**, 62 (2024), arXiv:2308.09469 [astro-ph.HE].
- [42] G. Raaijmakers, S. K. Greif, K. Hebeler, T. Hinderer, S. Nisanke, A. Schwenk, T. E. Riley, A. L. Watts, J. M. Lattimer, and W. C. G. Ho, *Astrophys. J. Lett.* **918**, L29 (2021), arXiv:2105.06981 [astro-ph.HE].
- [43] Z. Hu, Y. Gao, R. Xu, and L. Shao, *Phys. Rev. D* **104**, 104014 (2021), arXiv:2109.13453 [gr-qc].
- [44] M. R. Kennedy *et al.*, *Mon. Not. Roy. Astron. Soc.* **512**, 3001 (2022), arXiv:2202.05111 [astro-ph.HE].
- [45] Z. Miao, Y. Zhu, A. Li, and F. Huang, *Astrophys. J.* **936**, 69 (2022), arXiv:2204.05560 [astro-ph.HE].
- [46] S. Shawqi and S. M. Morsink, "Interpreting mass and radius measurements of neutron stars with dark matter halos," (2024), arXiv:2406.03332 [astro-ph.HE].
- [47] R. E. Rutledge, L. Bildsten, E. F. Brown, G. G. Pavlov, and V. E. Zavlin, *Astrophys. J.* **559**, 1054 (2001), arXiv:astro-ph/0105319.
- [48] R. C. Tolman, *Phys. Rev.* **55**, 364 (1939).
- [49] J. R. Oppenheimer and G. M. Volkoff, *Phys. Rev.* **55**, 374 (1939).
- [50] F. Sandin and P. Ciarcelluti, *Astropart. Phys.* **32**, 278 (2009), arXiv:0809.2942 [astro-ph].
- [51] C. Munoz, *Int. J. Mod. Phys. A* **19**, 3093 (2004), arXiv:hep-ph/0309346.
- [52] S. L. Shapiro and S. A. Teukolsky, *Black Holes, White Dwarfs, and Neutron Stars: The Physics of Compact Objects* (1983).
- [53] A. Akmal and V. R. Pandharipande, *Phys. Rev. C* **56**, 2261 (1997), arXiv:nucl-th/9705013.
- [54] H.-B. Li, Y. Gao, L. Shao, R.-X. Xu, and R. Xu, *Mon. Not. Roy. Astron. Soc.* **516**, 6172 (2022), arXiv:2206.09407 [gr-qc].
- [55] A. B. Henriques, A. R. Liddle, and R. G. Moorhouse, *Phys. Lett. B* **251**, 511 (1990).

- [56] P. Jetzer, *Phys. Lett. B* **243**, 36 (1990).
- [57] T. E. Riley *et al.*, *Astrophys. J. Lett.* **918**, L27 (2021), [arXiv:2105.06980 \[astro-ph.HE\]](#).
- [58] T. Salmi *et al.*, (2024), [arXiv:2406.14466 \[astro-ph.HE\]](#).
- [59] P. Amaro-Seoane, J. Barranco, A. Bernal, and L. Rezzolla, *JCAP* **11**, 002 (2010), [arXiv:1009.0019 \[astro-ph.CO\]](#).
- [60] D. Choudhury *et al.*, *Astrophys. J. Lett.* **971**, L20 (2024), [arXiv:2407.06789 \[astro-ph.HE\]](#).
- [61] V. Doroshenko, V. Suleimanov, G. Pühlhofer, and A. Santangelo, *Nature Astron.* **6**, 1444 (2022).
- [62] H. O. Silva and N. Yunes, *Phys. Rev. D* **99**, 044034 (2019), [arXiv:1808.04391 \[gr-qc\]](#).
- [63] R. Xu, Y. Gao, and L. Shao, *Phys. Rev. D* **102**, 064057 (2020), [arXiv:2007.10080 \[gr-qc\]](#).
- [64] M. C. Miller, F. K. Lamb, and G. B. Cook, *Astrophys. J.* **509**, 793 (1998), [arXiv:astro-ph/9805007](#).
- [65] S. M. Morsink, D. A. Leahy, C. Cadeau, and J. Braga, *Astrophys. J.* **663**, 1244 (2007), [arXiv:astro-ph/0703123](#).
- [66] J. Poutanen and A. M. Beloborodov, *Mon. Not. Roy. Astron. Soc.* **373**, 836 (2006), [arXiv:astro-ph/0608663](#).
- [67] G. B. Rybicki, *Radiative Processes in Astrophysics* (Wiley-VCH, 2004).
- [68] K. R. Pechenick, C. Ftaclas, and J. M. Cohen, *Astrophys. J.* **274**, 846 (1983).
- [69] S. Bogdanov, J. E. Grindlay, and G. B. Rybicki, *Astrophys. J.* **689**, 407 (2008), [arXiv:0801.4030 \[astro-ph\]](#).
- [70] B. P. Abbott *et al.* (LIGO Scientific, Virgo), *Phys. Rev. Lett.* **119**, 161101 (2017), [arXiv:1710.05832 \[gr-qc\]](#).
- [71] S. Bogdanov *et al.*, *Astrophys. J. Lett.* **887**, L26 (2019), [arXiv:1912.05707 \[astro-ph.HE\]](#).
- [72] M. T. Wolff *et al.*, *Astrophys. J. Lett.* **918**, L26 (2021), [arXiv:2105.06978 \[astro-ph.HE\]](#).
- [73] X. Li, F. Wang, and K. S. Cheng, *JCAP* **10**, 031 (2012), [arXiv:1210.1748 \[astro-ph.CO\]](#).
- [74] C. G. Boehmer and T. Harko, *JCAP* **06**, 025 (2007), [arXiv:0705.4158 \[astro-ph\]](#).
- [75] M. Mariani, C. Albertus, M. del Rosario Alessandroni, M. G. Orsaria, M. A. Perez-Garcia, and I. F. Ranea-Sandoval, *Mon. Not. Roy. Astron. Soc.* **527**, 6795 (2024), [arXiv:2311.14004 \[astro-ph.HE\]](#).